Energy 161 (2018) 1028–1041

Contents lists available at ScienceDirect

Energy

journal homepage: www.elsevier.com/locate/energy

Study of the turbulent flow in a newly solar air heater test bench with natural and forced convection modes

Badis Bakri [a, *], Oumaima Eleuch [a], Ahmed Ketata [a], Slah Driss [a], Zied Driss [a], Hani Benguesmia [b]

[a] Laboratory of Electro-Mechanic Systems (LASEM), National School of Engineers of Sfax (ENIS), University of Sfax, B.P. 1173, Km 3.5RoadSoukra, 3038, Sfax, Tunisia
[b] Faculty of Technologies, University of M'sila, Algeria

ARTICLE INFO

Article history:
Received 14 March 2018
Received in revised form
21 July 2018
Accepted 27 July 2018
Available online 2 August 2018

Keywords:
Solar air heater
Test bench
Tow passages
Box prototype
Aerodynamic structure

ABSTRACT

In this work, the turbulent flow was studied in a new SAH (solar air heater) test bench. Particularly, we have considered the natural and the forced convection modes. The used test bench is composed by two passages separated by an absorber and powered by a fan working in a delivery mode, placed in the inlet side the insulation, for the forced convection mode. On this system, a glass is hanging on the front side and an absorber is inserted inside. On the glass side, it is connected to the box prototype through a pipe. The hot air flow is routed towards the box prototype. Two circular holes, are located in the same face of the box prototype. The inlet hole allows the hot air supply. However, the outlet hole allows its escape into the ambient environment. By using the ANSYS Fluent 17.0 software, the Navier-Stokes equations coupled with the standard k-ω turbulence model were solved. The numerical results were compared with our experimental data, established in the second passage of the SAH test bench. The good agreement confirms the validity of the numerical method. The range of temperatures is very useful in many applications such as industrial and domestic applications.

1. Introduction

SAH (solar air heater) systems are increasingly requested in order to obtain a controlled temperature, in particular during cold periods. Solar energy refers to all the techniques where SAH system can be used on site, since it is cheap and simple. It is directly related to building techniques that save energy for heating. The objective is to minimize energy consumption with the use of renewable energy [1–3]. In this context, Yang et al. [1] designed a SAH with offset strip fins optimized by numerical modeling. Then, a series of experiments based on ASHRAE Standard 93–2003 was conducted to test the detailed thermal performance of the heater in the light of time constant, thermal efficiency, incident angle modifier and the synthetical resistance coefficient. Altaa et al. [2] compared three different types of designed flat-plate SAH, two having fins and the other without fins. One of the heaters with a fin had a single glass cover and the others had double glass covers. Based on the energy output rates, heater with double glass covers and fins is more effective and the difference between the input and output air temperature is higher than of the others. Zukowski [3] presented a novel construction of a forced SAH based on a confined single slot jet of air impinging on the flat surface of an absorber plate. The results of experimental research showed that the efficiency of energy conversion ranged from 66% up to 90%. El-Sebaii et al. [4] developed a comparison between the measured outlet temperatures of flowing air, temperature of the absorber plate and output power of the double pass-finned and v-corrugated plate SAH. The results showed that the double pass v-corrugated plate SAH is 9.3–11.9% more efficient compared to the double pass-finned plate SAH. Wazed et al. [5] confirmed that the fabricated SAH is working efficiently. The maximum room temperature and the temperature difference from ambient are 45.5 °C and 12.25 °C for forced circulation and 41.75 °C and 8.5 °C for natural circulation respectively. Sopian et al. [6] confirmed that the addition of the porous media in the second channel of the double-pass solar collector increases the performance of the collector. The experimental validation shows that the theoretical simulation and experimental data were in close agreement with each other. The efficiency of the double pass solar

* Corresponding author.
E-mail address: badisbakri@yahoo.fr (B. Bakri).

https://doi.org/10.1016/j.energy.2018.07.187
0360-5442/

collector with porous media is about 60–70%. Esen et al. [7] presented an energy analysis for a novel flat plate SAH with several obstacles and without obstacles. The analysis of the results confirmed that the optimal value of the efficiency is a middle level of absorbing plate in flow channel duct for all operating conditions. The double-flow collector supplied with obstacles appears significantly better than without obstacles. The results showed that the largest irreversibility is occurring at the flat plate collector and without obstacles in which collector efficiency is smallest. Ozgen et al. [8] experimentally investigated a device for inserting an absorbing plate made of aluminum cans into the double-pass channel in a flat-plate SAH. Three different absorber plates had been designed and tested for experimental study. The highest efficiency had been obtained for an air mass flow rates of 0.05 kg/s. Chen and Zhang [9] studied the basic characteristics of solar thermal conversion using supercritical CO2–dimethyl ether (DME) natural convection. They observed that the introduction of DME has successfully reduced the operation pressure and the increase in DME fraction leads to further reduction. Zhang et al. [10] presented the basic characteristics of solar thermal conversion using supercritical CO2 natural convection. They observed that the collecting efficiency increases with the comprehensive coefficient and this pattern is contrary to that of water based system. Chen and Zhang [11] tested a novel solar thermal conversion and water heater system achieved by supercritical CO2 natural circulation. They observed that the supercritical CO2 pipe flow with Reynolds number higher than 6700 and the CO2 fluid temperature in the heat exchanger can be as high as 80 °C. Hassen and Abouelfadhl [12] studied the performance of double pass SAH with different absorber plate configurations. Based on the results of several experimental studies, Allam and Kim [13] confirmed that the double pass of SAH achieves better performance than single-pass. According to the results of Goodarzi and Nouri [14], the wall temperature in the double-pass heat exchanger presents better uniformity compared to the usual one. Indeed, the power consumption for handling the specified volumetric flow rate is greater than those required within the others considered cases. Singh and Dhiman [15] indicated that the use of the double pass SAH significantly increases the thermal performance as compared to another considered system.

Based on the literature reviews, we have introduced a new SAH with two passages connected to a box prototype. The choice of this test bench is based on the anterior studies. However, the design of the all parts and the considered geometrical arrangements present newly solutions; which can be updated as required. For example, the shape design, the dimensions and the position of the different compounds like the absorber, the collector, the diffuser and the holes can be updated and changed to develop new experiences and to look on the optimized configuration. In the present work, we are limited on the experimental validation of the numerical method used to study the turbulent flow in our newly SAH test bench with natural and forced convection. Following this work, several numerical simulations will be developed in order to propose the optimized geometrical parameters. This preliminary work is very useful because it presents the first step, which aims to make a complete optimization on the various components of the same SAH system. This approach has not been undertaken before completely. In fact, in most anterior works, studies are done on some parameters separately and each study is done on a new separated system; which will not lead to a complete solution.

2. Experimental device

Fig. 1 shows the experimental device consisting of a new SAH test bench consisting of two passages SAH separated by an absorber

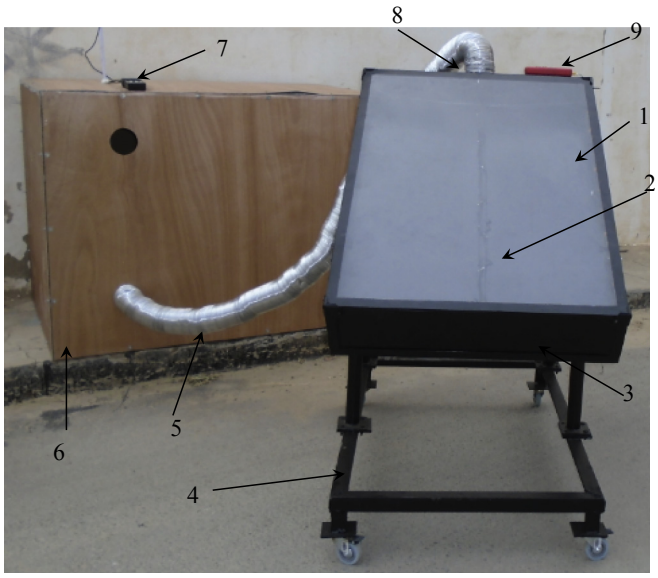

N°	Designation
1	Glass cover
2	Absorber plate
3	Insulation
4	Mobile base
5	Duct
6	Box prototype
7	Anemometer
8	Fan
9	Digital thermometer

Fig. 1. Solar air heater test bench.

and powered by a fan working in a delivery mode and placed in the inlet, side the insulation. On the glass side, it is connected to the box prototype through a pipe. To study the behavior of our SAH system, we measured the temperature and the air velocities in different controlled points.

To measure the air velocity, we have used the hot-wire anemometer type AM 4204 since it is simple and offers the greatest flexibility of use and high resolution. The characteristics of the anemometer are summarized in Table 1. By dropping the probe in the appropriate position, the velocity value can be read directly from the digital screen. To measure the temperature, we have used the Uni Trend Model UT325 Thermometer, which is a digital thermometer designed to use external J, K, T, E, R, S and N type thermocouples as temperature sensors. This instrument has a software and USB data cable allowing the connection of the thermometer to our laptop and the continuous data transfer. The characteristics of

Table 1
Characteristics of the anemometer.

Description	Anemometer type AM 4204
Manufacturer	Lutron
Probe type	Telescopic
Measurement parameters	Air velocity, temperature, gaz flow
Resolution	Air velocity 0,1 m s^{-1}
	Temperature 0,1 °C
Precision	Air velocity 5%
	Temperature ±0,8 °C
Measuring range	Air velocity from 0,2–20 m s^{-1}
	Temperature from −20 °C to +70 °C

the digital thermometers are given in Tables 2 and 3. The geometrical arrangements of the computational domain are presented in Fig. 2. It is composed of two domains separated by a circular pipe with a diameter d = 100 mm. The first one is the SAH with a height $h_s = 194$ mm and a width $W_s = 778$ mm. On this system, a glass is hanging on the front side with a length $L_g = 1000$ mm and an absorber is inserted inside with a length $L_a = 1086$ mm. The hot air flow is routed towards the box prototype with a length $L_b = 1500$ mm, a height $H_b = 1100$ mm and a width $W_b = 1000$ mm. Two circular holes, with a distance $h_2 = 900$ mm, are located in the same face of the box prototype. The inlet hole, placed in the altitude $h_1 = 250$ mm and a longitude $L_1 = 300$ mm, allows the hot air supply. However, the outlet hole allows its escape in the ambient environment.

3. Numerical model

In this section, the mathematical formulation, the boundary conditions and the meshing, used to model the considered SAH system, are presented.

3.1. Mathematical formulation

The air flow modeling is governed by the continuity equation, the momentum equations and the energy equation [16–18]. Substituting expressions into instantaneous equations and taking time average yields, we can write in the Cartesian system:

$$\frac{\partial \rho}{\partial t} + \frac{\partial}{\partial x_i}(\rho u_i) = 0 \tag{1}$$

$$\frac{\partial}{\partial t}(\rho u_i) + \frac{\partial}{\partial x_j}(\rho u_i u_j) = -\frac{\partial p}{\partial x_i} + \frac{\partial}{\partial x_j}\left[\mu\left(\frac{\partial u_i}{\partial x_j} + \frac{\partial u_j}{\partial x_i} - \frac{2}{3}\delta_{ij}\frac{\partial u_i}{\partial x_i}\right)\right] + \frac{\partial}{\partial x_j}\left(-\rho\overline{u'_i u'_j}\right) \tag{2}$$

These equations are the RANS (Reynolds-averaged Navier-Stokes) equations, which present the same form as the instantaneous equations. The new terms introduce the Reynolds stresses $-\rho\overline{u'_i u'_j}$ should be modeled to close the RANS equation.

The used method applies the Boussinesq hypothesis relating the Reynolds stresses with the mean velocity gradients:

$$-\rho\overline{u'_i u'_j} = \mu_t\left(\frac{\partial \mu_i}{\partial x_j} + \frac{\partial \mu_j}{\partial x_i}\right) - \frac{2}{3}\left(\rho k + \mu_t\frac{\partial \mu_k}{\partial x_k}\right)\delta_{ij} \tag{3}$$

This hypothesis is undertaken in different turbulence models. This approach presents low computational cost compared to other numerical methods [19]. By using the standard k-ω turbulence model, the turbulent viscosity μ_t is defined by:

$$\mu_t = \alpha^*\frac{\rho k}{\omega} \tag{4}$$

For the correction of the low-Reynolds number, α^* is calculated as follows:

$$\alpha^* = \alpha^*_\infty\left(\frac{\alpha^*_0 + Re_t/R_k}{1 + Re_t/R_k}\right) \tag{5}$$

Where:

$$Re_t = \frac{\rho k}{\mu\omega} \tag{6}$$

$$R_k = 6 \tag{7}$$

$$\alpha^*_0 = \frac{\beta_i}{3} \tag{8}$$

$$\beta_i = 0.072 \tag{9}$$

However, for the high-Reynolds number form of the k-ω model:

$$\alpha^* = \alpha^*_\infty = 1. \tag{10}$$

For the low-Reynolds number, the standard k-ω turbulence model incorporates modifications [19]. With this model, the turbulent kinetic energy k and the specific dissipation rate ω are written as follows:

$$\frac{\partial}{\partial t}(\rho k) + \frac{\partial}{\partial x_i}(\rho k u_i) = \frac{\partial}{\partial x_i}\left(\Gamma_k\frac{\partial k}{\partial x_j}\right) + G_k - Y_k + S_k \tag{11}$$

$$\frac{\partial}{\partial t}(\rho\omega) + \frac{\partial}{\partial x_i}(\rho\omega u_i) = \frac{\partial}{\partial x_j}\left(\Gamma_\omega\frac{\partial \omega}{\partial x_j}\right) + G_\omega - Y_\omega + S_\omega \tag{12}$$

Constants of the standard k-ω turbulence model are presented in Table 4.

The energy equation is written in the following form:

$$\frac{\partial}{\partial t}(\rho E) + \nabla\cdot(\vec{v}(\rho E + p)) = \nabla\cdot\left(K_{eff}\nabla T - \sum_j h_j\vec{J}_j + \left(\bar{\bar{\tau}}_{eff}\cdot\vec{v}\right)\right) + S_h \tag{13}$$

Table 3
Main specifications of the digital thermometer.

Basic Functions	UT325
Temperature −200.0 °C to +1372 °C (K-Type) −328.0 °F to +2501 °F	✓
Temperature −210.0 °C to +1200 °C (J-Type) −346.0 °F to +2192 °F	✓
Temperature Best Accuracy	K, J, T, E type: 0.2% ± 0.6 °C R, S type: 0.2% ± 2 °C N type: 0.2% ± 1.5 °C
Display Resolution	0.1 °C
T1, T2 input	✓
High/Low Signal Output	✓
User Self-Calibration	✓
Data Logging	100

Table 2
General characteristics of the digital thermometer.

Power	USB (Auto Double With Display Backlight) or 9 V Battery (6F22)
LCD Size	30 × 32 mm
Product Net Weight	270 g
Product Size	175 × 85 × 30 mm
Standard Accessories	Battery, English Manual, USB Cable, Software, K Type Temperature Probe

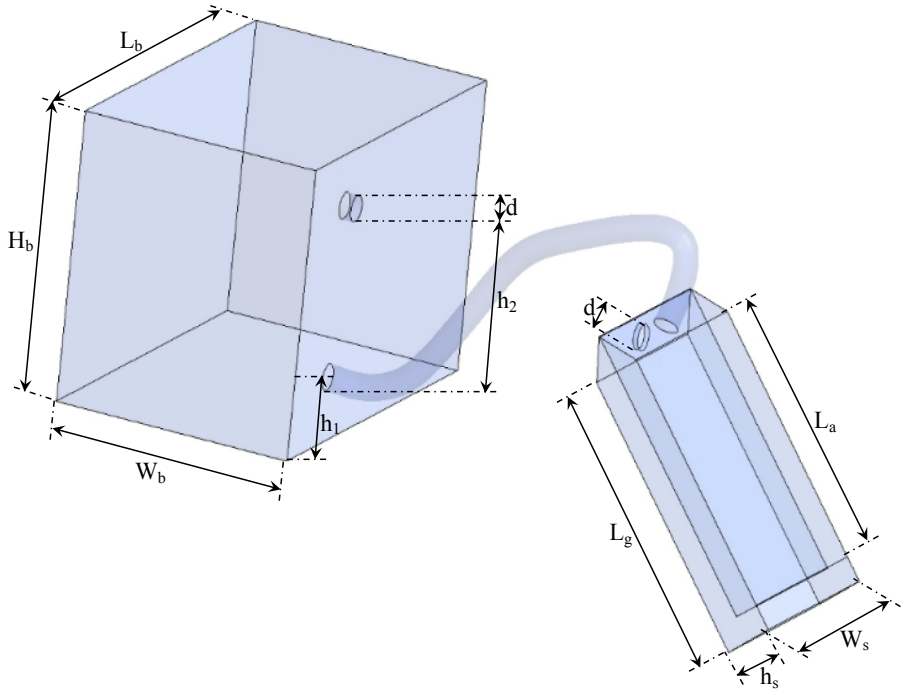

Parameters	Value (mm)
Length of the box prototype L_b	1500
Height of the box prototype H_b	1100
Width of the box prototype W_b	1000
Length of the absorber L_a	1086
Length of the glass L_g	1000
Width of the SAH W_s	778
Height of the SAH h_s	194
Position of the holes inlet h_1	250
Distance between the two holes h_2	900
Diameters of the holes d	100

Fig. 2. Geometrical arrangements.

Table 4
Standard k-ω turbulence model constants.

α_0	α_∞	α^*_∞	R_ω	R_k	σ_k	σ_ω
1/9	1.9	1.0	2.95	6.0	2.0	2.0

Where K_{eff} is the effective conductivity and $\overrightarrow{J}_j$ is the diffusion flux of species j.

The deviatoric stress tensor $(\tau_{ij})_{eff}$ and the total energy E are defined as:

$$(\tau_{ij})_{eff} = \mu_{eff}\left(\frac{\partial u_j}{\partial x_i} + \frac{\partial u_i}{\partial x_j}\right) - \frac{2}{3}\mu_{eff}\frac{\partial u_k}{\partial x_k}\delta_{ij} \tag{14}$$

$$E = h - \frac{p}{\rho} + \frac{V^2}{2} \tag{15}$$

For ideal gases, the sensible enthalpy h is defined as:

$$h = \sum_j Y_j h_j \tag{16}$$

However, for incompressible flows it is defined as:

$$h = \sum_j Y_j h_j + \frac{p}{\rho} \tag{17}$$

Where Y_j is the mass fraction of species j.

The sensible enthalpy calculation depends on the solver and models in use and the value used for T_{ref}:

$$h_j = \int_{T_{ref}}^{T} c_{p\cdot j}\, dT \tag{18}$$

The radiative transfer equation (RTE) is defined at position $\overrightarrow{r}$ and in the direction $\overrightarrow{s}$ as follows:

$$\frac{dI(\overrightarrow{r},\overrightarrow{s})}{ds} + (a+\sigma_s)I(\overrightarrow{r},\overrightarrow{s}) = an^2\frac{\sigma T^4}{\pi} + \frac{\sigma_s}{4\pi}\int_0^{4\pi} I(\overrightarrow{r},\overrightarrow{s}')\varphi(\overrightarrow{s},\overrightarrow{s}')d\Omega' \tag{19}$$

Where:

$\vec{r}$: position vector.
$\vec{s}$: direction vector.
$\vec{s}'$: scattering direction vector.
s: path length.
a: absorption coefficient.
n: refractive index.
σ_s: scattering coefficient.
σ: Stefan-Boltzmann constant equal to 5.669 10^{-8} W m^{-2}.K^{-4}.
I: radiation intensity.
T: temperature.
φ: phase function.
Ω': solid angle.

The DO model considers the RTE as a field equation [19] and it is written as follows:

$$\nabla\cdot[I(\vec{r},\vec{s})\vec{s}]+(a+\sigma_s)I(\vec{r},\vec{s})=an^2\frac{\sigma T^4}{\pi}+\frac{\sigma_s}{4\pi}\int_0^{4\pi}I(\vec{r},\vec{s}')\varphi(\vec{s}\cdot\vec{s}')d\Omega' \quad (20)$$

By using a gray-band model and for the spectral intensity $I_\lambda(\vec{r},\vec{s})$[19], the RTE is written as follows:

$$\nabla\cdot[I_\lambda(\vec{r},\vec{s})\vec{s}]+(a_\lambda+\sigma_s)I_\lambda(\vec{r},\vec{s})=a_\lambda I_{b\lambda}+\frac{\sigma_s}{4\pi}\int_0^{4\pi}I_\lambda(\vec{r},\vec{s}')\varphi(\vec{s},\vec{s}')d\Omega' \quad (21)$$

Where:
I_λ: spectral intensity.
λ: the wavelength.
a_λ: the spectral absorption coefficient.
$I_{b\lambda}$: the black body intensity given by the Planck function.

By summation over the wavelength bands [19], the total intensity $I(\vec{r},\vec{s})$ is computed as follows:

$$I(\vec{r},\vec{s})=\sum_k I_{\lambda_k}(\vec{r},\vec{s})\Delta\lambda_k \quad (22)$$

By integration over a control volume [19], the discrete energy equation can be written:

$$\sum_{j=1}^{N}\mu_{ij}^T T_j-\beta_i^T T_i=\alpha_i^T\sum_{k=1}^{L}I_i^k\omega_k-s_i^T+s_i^h \quad (23)$$

In these conditions:

$$\alpha_i^T=K_a\Delta V_i \quad (24)$$

$$\beta_i^T=16K_a\sigma T_i^{*3}\Delta V \quad (25)$$

$$s_i^T=12K_a\sigma T_i^{*4}\Delta V \quad (26)$$

Where:
K_a: absorption coefficient.
ΔV : control volume.

The coefficient μ_{ij}^T and the source term s_i^h are due to the discretization of the convection and diffusion terms as well as the non-radiative source terms.

In these conditions, the convective heat transfer coefficient h_{cga}(W.m^{-2}.K^{-1}) for air flowing over the outside surface of the glass cover is proposed by McAdams [20] as follows:

$$h_{cga}=5.7+3.8V \quad (27)$$

Where V is the air velocity (m.s^{-1}).

For the SAH test bench, the energy efficiency is written as follows:

$$\eta=\frac{\dot{m}C_p(T_{out}-T_{in})}{IA} \quad (28)$$

Where:
$\dot{m}$: Mass flow rate (kg.s^{-1}).
C_p: Specific heat capacity of the air at constant pressure (J.kg^{-1}.K^{-1}).
T_{out}: Outlet temperature (K).
T_{in}: Inlet temperature (K).
I: Solar radiation (W.m^{-2}).
A: Area of the SAH (m^2).

3.2. Boundary conditions

A boundary condition is required anywhere fluid enters or exits the system and can be set as a pressure inlet, mass flow inlet, interior, internal or interface. The general interpretation was given on the basis of numerical simulation of the SAH. A physical model was simulated using ANSYS Fluent 17.0, based on the geometrical dimensions of the SAH. Wall boundary was applied to the SAH with a heat flux of value equal zero to obtain the adiabatic wall. Wall boundary was used for the absorber and the glass and convective heat transfer option was applied for different parts of these devices. For the outlet pressure, a value of p = 101325 Pa is set. This means that at this opening, the fluid exits the model to an area of static atmospheric pressure condition. For the natural convection mode, a value of p = 101325 Pa is set in the pressure inlet. This means that at this opening the fluid enters and exits the model to an area of static atmospheric pressure condition. However, for the forced convection mode a velocity inlet, equal to V = 3 m s^{-1}, has been considered. Using the solar calculator of the discrete ordinates (DO), we have defined all the considered parameters of the radiation model with fair weather conditions. For the global position, we have introduced the longitude, the latitude and the time zone. For the date and time, we have indicated the day, the month, the hour and the minute. Also, we have specified the north and the east of the mesh orientation. In our test bench, the lateral surfaces of the solar air heater system and the box prototype were fabricated by the wood with a conductivity equal to λ = 0.1 W m^{-1}.K^{-1} [21]. By considering it adequate for thermal insulation, we have used adiabatic wall in our simulation.

3.3. Meshing

The automatically generated mesh is usually appropriate and intricates problems with thin and small. Geometrical and physical features can result in an extremely high number of cells, for which the computer memory is too small. Meshing options allow us to manually adjust the computational mesh to the solved problems features to resolve them better. In this application, we have adopted a refined model consisting of a number of cells equal to N = 1578369 cells. This meshing gives the lower numerical diffusion inside the SAH with an unstructured and tetrahedral meshing as presented in Fig. 3. To simulate our considered application referring to the turbulent flow in a solar air heater test bench at t = 14 h, we considered the CFD results with a calculations time equal to t = 10 day. In these conditions, the residual values referring to the numerical parameters are equal to 10^{-6}. In these simulations,

the used computer is characterized by a processor with an Intel (R) Xeon (R) CPU E3-1226v3 @ 3.30 GHz, an installed memory (RAM) of 12.0 GB (11.7 GB usable) and a system type of 64-bit operating system, ×64 processor.

4. Results and discussion

The distribution of the velocity fields, the temperature, the Do irradiation, the total pressure, the turbulent kinetic energy, the specific turbulent dissipation rate and the turbulent viscosity are presented in this section. In the natural convection mode, the Reynolds number is evaluated to be equal to Re = 1300. However, it is equal to Re = 20000 in the forced convection mode.

4.1. Comparison with experimental results

Figs. 4 and 5 compare the numerical results of the temperature and velocity profiles in the second channel superposed with our experimental results for the natural and the forced convection modes at t = 14 h in August 2017. According to these results, a different appearance between the curves has been observed. In fact, for the natural convection mode, the temperature values vary between T = 343 K and T = 347 K. However, for the forced convection mode, the temperature presents low values varying between T = 324 K and T = 337 K. Contrariwise, the magnitude velocity values vary between V = 0.07 m s^{-1} and V = 0.24 m s^{-1} for the natural convection mode and between V = 0.3 m s^{-1} and V = 1.2 m s^{-1} for the forced convection mode, which presents height values. In these two cases, the maximum values of the magnitude velocity are obtained in the hole outlet of the SAH. The comparison of the numerical results with our experimental data, picked up at t = 14 h, presents a good agreement with a gap equal to 6%. These results confirm the validity of our numerical method.

4.2. Velocity fields

Fig. 6 compares the velocity fields distribution for the natural and the forced convection modes at t = 14 h in the longitudinal plane of the SAH supplying the box prototype. According to these results, it is clear that the choice of the convection mode presents a direct effect on the velocity field distribution. In fact, for the natural

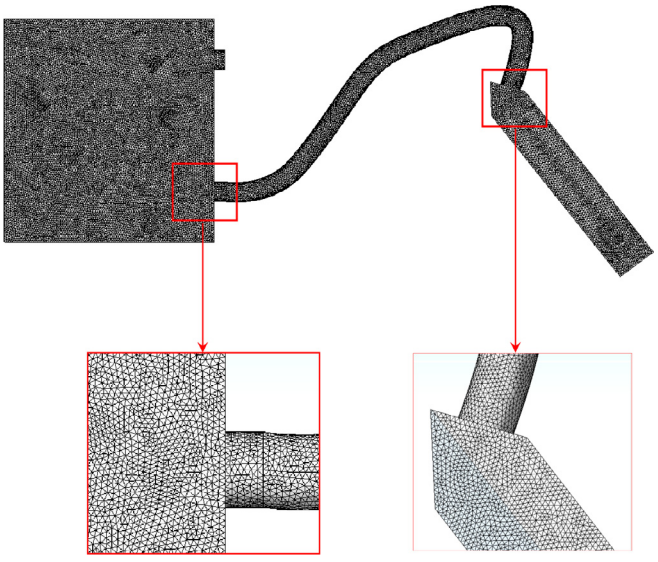

Fig. 3. Meshing of the computational domain.

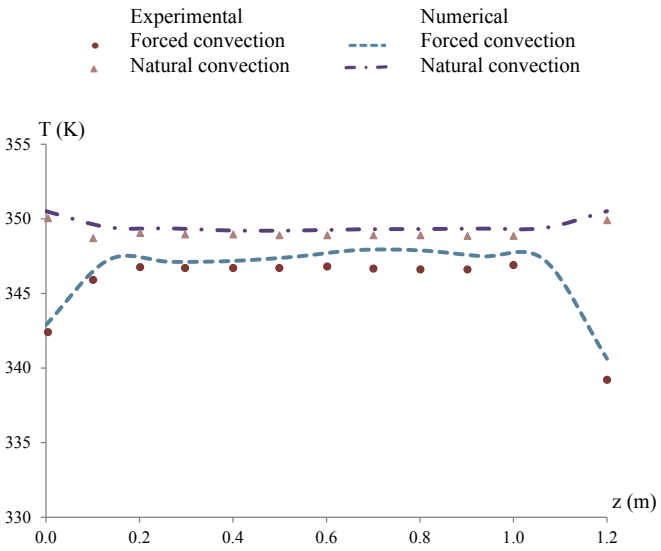

Fig. 4. Profiles of the temperature in the second channel.

convection mode, it is clear that the velocity inlet presents a weak value equal to V = 0.2 m s^{-1}. At the first passage, an increase of the flow has been observed in the first passage of the SAH. The maximum value equal to V = 0.51 m s^{-1} has been noted at the beginning of the flow. From the middle of the first passage of the SAH, the velocity drops slowly until the bottom of the SAH. At this level, the velocity value is equal to V = 0.15 m s^{-1}. Indeed, different recirculation zones have been observed along the second passage of the SAH. At this level, the velocity value is very weak and it is about V = 0.51 m s^{-1}. Crossing the pipe separating the SAH from the box prototype, the velocity reaches V = 0.38 m s^{-1}. Via the box prototype hole inlet, a discharge area invaded the reverse wall. In this side, the velocity changes his direction and two axial flows have been observed. The first ascending flow is responsible for the recirculation zone appeared in the whole area of the box prototype. This movement continues until the exit of the air flow through the hole outlet and reaches the maximum value equal to V = 0.28 m s^{-1}. The second descending flow is due to the dead zone appeared in the down area. Globally, the averaged velocity value is about V = 0.1 m s^{-1} in the discharge area.

However, for the forced convection mode, the inlet velocity is governed by the boundary condition defined by V = 3 m s^{-1}. In the first passage, a decrease in the flow has been observed and a recirculation zone was created. This phenomenon is more prominent during the transition of the flow to the second passage. In this side, the flow becomes uniform until the exit of the SAH. Indeed, the velocity reaches a very important value equal to V = 5.19 m s^{-1}. Via the pipe separating the SAH from the box prototype, a discharge area appears in the hole inlet and invaded the reverse wall. At this level, the velocity changes his direction and two axial flows have been observed. The first ascending flow is responsible for the recirculation zone appeared in the wholes area of the box prototype. This movement continues until the exit of the air flow through the hole outlet and reaches the maximum value equal to V = 4 m s^{-1}. The second descending flow is due to the dead zone appeared in the down area. Globally, the averaged velocity value is about V = 1.5 m s^{-1} in the discharge area. Elsewhere, the averaged velocity presents a very low value.

4.3. Temperature

Fig. 7 compares the temperature distribution for the natural and

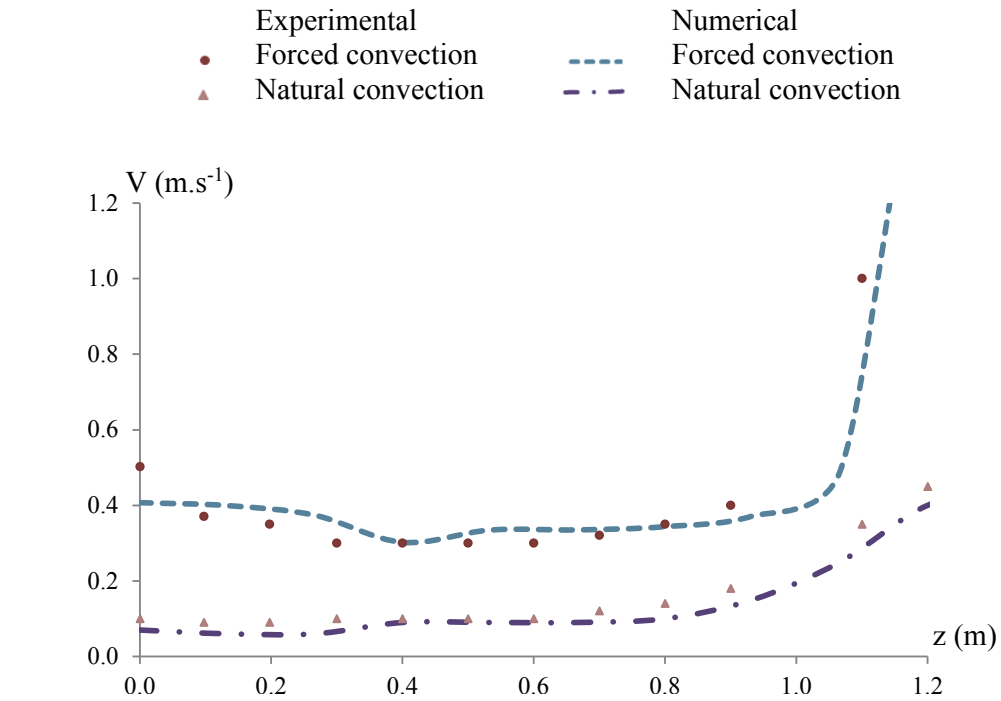

Fig. 5. Profiles of the magnitude velocity in the second channel.

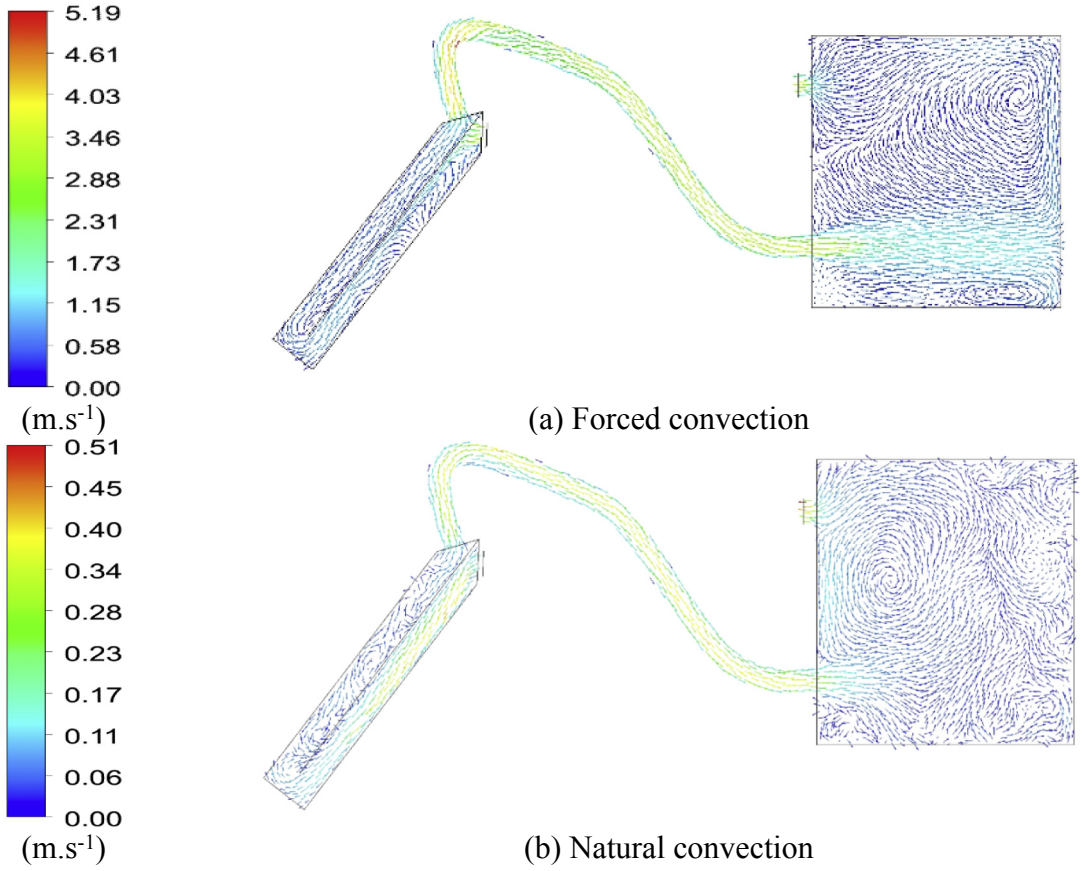

Fig. 6. Distribution of the velocity fields in the longitudinal plane.

the forced convection modes at t = 14 h in the longitudinal plane of the SAH supplying the box prototype. According to these results, it is clear that the choice of the convection mode presents a direct effect on the temperature distribution. In fact, for the natural convection mode, it has been noted that the inlet temperature is governed by the boundary condition defined by T = 308 K. This value increases immensely and reaches an average value equal to T = 342 K in the first passage and T = 350 K in the second passage. This fact can be explained by the air flow incoming at ambient temperature and flowing the channel between the absorber plate and the insulation, which start swarming up by the convection with the absorber. In the second passage, the temperature of the airflow is more important since the flowing between the glass and the absorber is affected by the solar radiations. Thereby, the box prototype is powered by a continuous air heater characterized by the maximum temperature value equal to T = 354 K. In the hole outlet of the box prototype, the temperature drops and reaches T = 308 K.

However, for the forced convection mode, it has been noted that the inlet temperature is governed by the boundary condition defined by T = 308 K. This value increases immensely and reaches an average value equal to T = 335 K in the first passage and T = 344 K in the second passage. This fact can be explained by the air flow incoming at ambient temperature and flowing the channel between the absorber plane and the insulation, which start swarming up by the convection with the absorber. In the second passage, the temperature of the airflow is more important since the flowing between the glass and the absorber is affected by the solar radiations. Thereby, the box prototype is powered by a continuous air heater characterized by the maximum temperature value equal to T = 347 K.

4.4. Distribution of the Do irradiation

Fig. 8 compares the Do irradiation distribution for the natural and the forced convection modes at t = 14 h in the longitudinal plane of the SAH supplying the box prototype. According to these results, it is clear that the choice of the convection mode presents a direct effect on the Do irradiation distribution. In fact, for the natural convection mode, it has been observed that the Do irradiation presents a low value equal to I = 2600 W m^{-2} in the SAH inlet. This value increases immensely and reaches the maximum value I = 3360 W m^{-2} near the absorber in the second mid-plane of the first passage of the SAH. In the second passage, a gradual decrease of the Do irradiation has been observed with an average value equal to I = 3220 W m^{-2}. The minimum value of the Do irradiation equal to I = 3200 W m^{-2} has been observed in the second mid-plane of the second passage of the SAH. From the inlet of the pipe, attached to the SAH, the Do irradiation reaches the maximum value equal to I = 3336 W m^{-2} in all the field of the box prototype. In the hole outlet of the box prototype, the Do irradiation drops and reaches I = 2460 W m^{-2}.

However, for the forced convection mode, it has been observed that the Do irradiation presents a low value equal to I = 2500 W m^{-2} in the inlet of the SAH. This value increases immensely and reaches the maximum value I = 3170 W m^{-2} near the absorber in the second mid-plane of the first passage of the SAH. In the second passage, a gradual decrease of the Do irradiation has been observed with an average value equal to I = 3000 W m^{-2}. The minimum value of the Do irradiation equal to I = 2650 W m^{-2} has been observed in the second mid-plane of the second passage of the SAH. From the inlet of the pipe, attached to

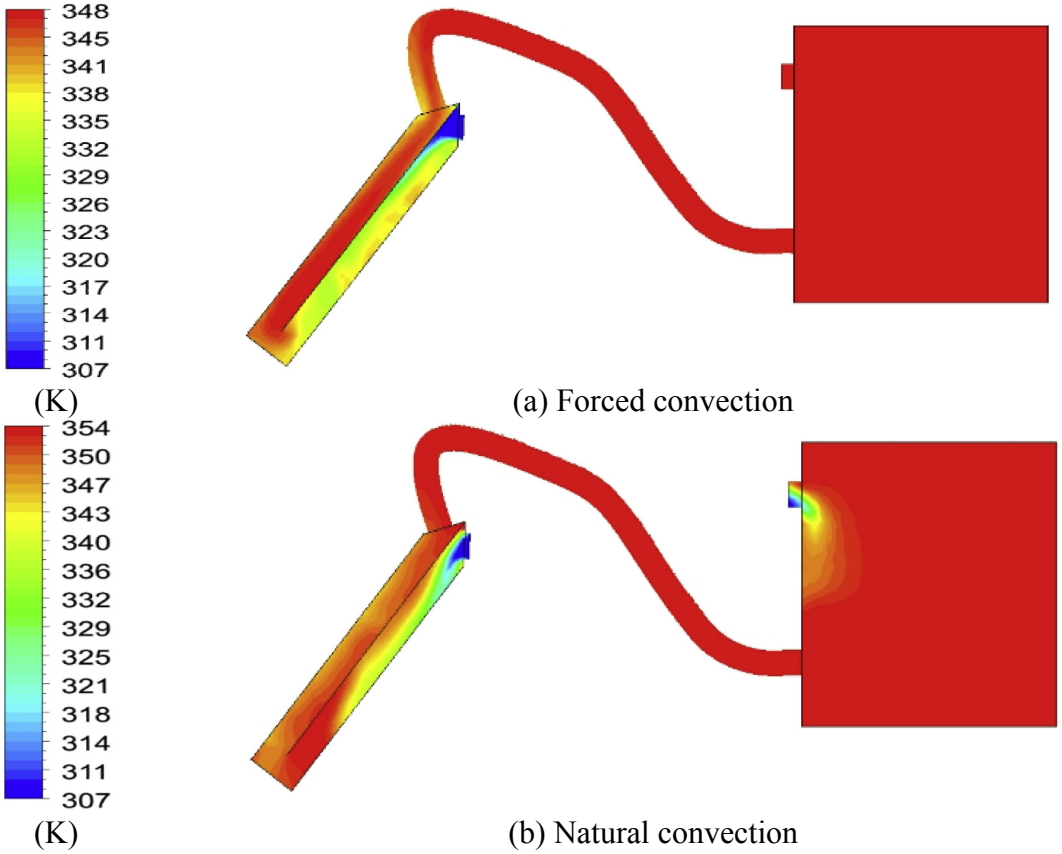

Fig. 7. Distribution of the temperature in the longitudinal plane.

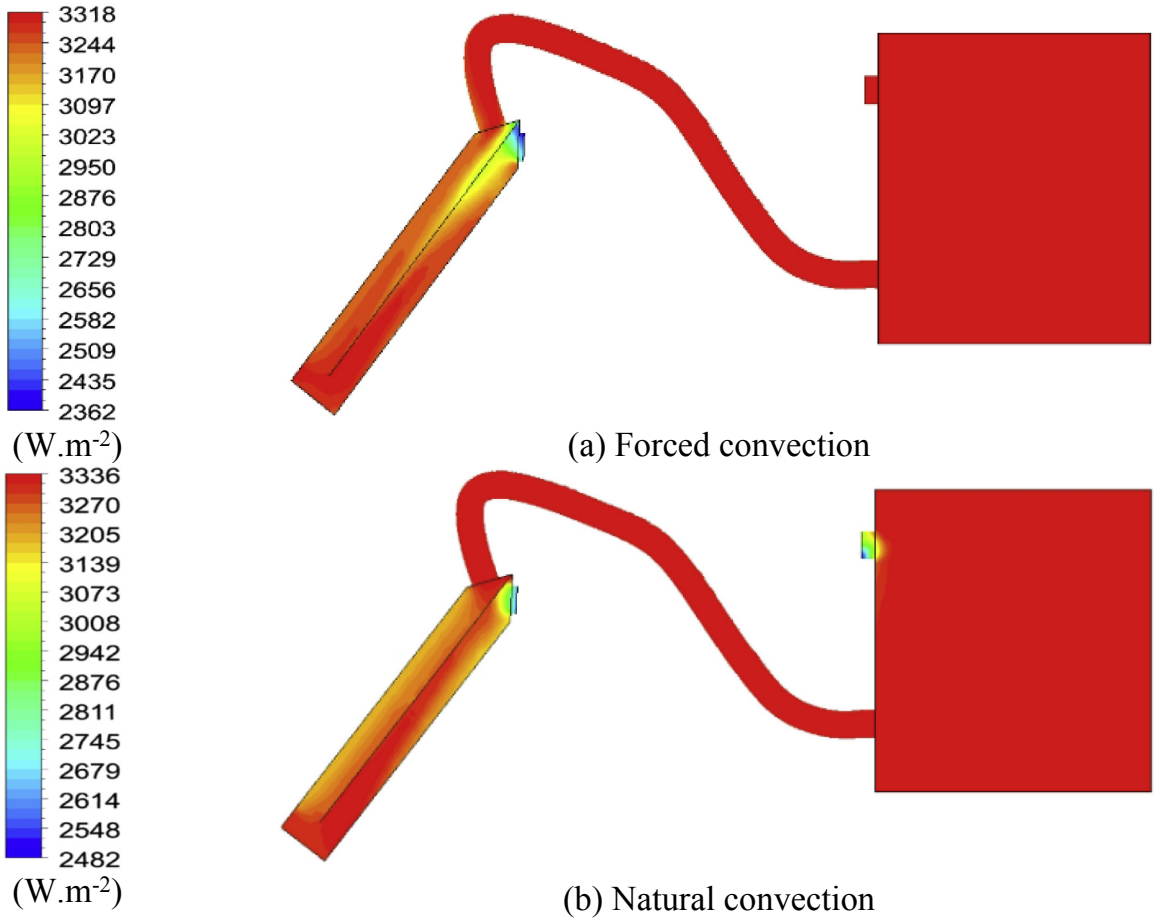

Fig. 8. Distribution of the Do Irradiation in the longitudinal plane.

the SAH, the Do irradiation reaches the maximum value equal to $I = 3318\ W\ m^{-2}$ in all the field of the box prototype.

4.5. Total pressure

Fig. 9 compares the total pressure distribution for the natural and the forced convection modes at $t = 14$ h in the longitudinal plane of the SAH supplying the box prototype. According to these results, it is clear that the choice of the convection mode presents a direct effect on the total pressure distribution. In fact, for the natural convection mode, it is clear that the total pressure inlet is governed by the boundary condition defined by the atmospheric pressure. Then, the relative total pressure decreases weakly at the bottom of the SAH and reaches $p = 0$ Pa. From this side, the relative total pressure increases slightly in the second passage of the SAH. At the exit of the second passage, the relative total pressure continues increasing along the pipe and reaches a value equal to $p = 1$ Pa at the first half part of the pipe separating the SAH from the box prototype. From the hole inlet of the box prototype roof, there is a slight increase of the relative total pressure until the box prototype roof. In this side, the maximum value of the relative total pressure is equal to $p = 2$ Pa. In the hole outlet of the box prototype, it is governed by the boundary condition defined by the atmospheric pressure.

However, for the forced convection mode, a compression zone characteristic of the maximum value of the relative total pressure has been observed in the collector inlet. Then, the relative total pressure decreases and presents a stabilized value, equal to $p = 41$ Pa, in the remaining domain of the two passage of the SAH. At the exit of the second passage, the relative total pressure continues decreasing along the pipe and reaches a value equal to $p = 22$ Pa in the inlet of the box prototype. Through the air advancement, the relative total pressure decreases quietly in the expulsion area, produced from the hole inlet and invaded until the reverse wall. This fact can be explained by the recirculation zone appeared in the wholes area of the box prototype. In the hole outlet, a depression zone characteristic of the minimum value, equal to $p = 2$ Pa, has been observed.

4.6. Turbulent kinetic energy

Fig. 10 compares the turbulent kinetic energy distribution for the natural and the forced convection modes at $t = 14$ h in the longitudinal plane of the SAH supplying the box prototype. According to these results, it is clear that the choice of the convection mode presents a direct effect on the turbulent kinetic energy distribution. In fact, for the natural convection mode, the turbulent kinetic energy presents a weak value in the collector inlet of the SAH. Through the first passage, the turbulent kinetic energy increases and reaches the maximum value at the second mid-plane and near the absorber. In this side, the maximum value of the turbulent kinetic energy is equal to $k = 0.1\ m^2\ s^{-2}$. At the exit of the first passage, the turbulent kinetic energy decreases before increasing in the second passage. In this side, the maximum value of the turbulent kinetic energy is equal to $k = 0.17\ m^2\ s^{-2}$. At the exit of the first passage, the turbulent kinetic energy decreases and

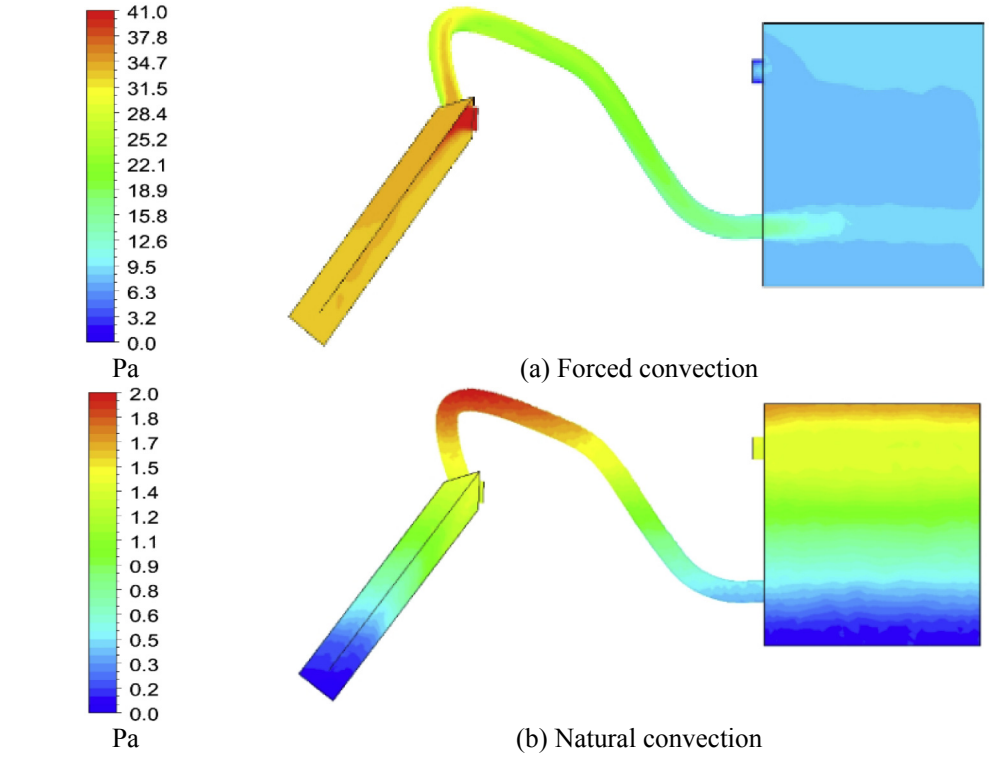

Fig. 9. Distribution of the total pressure in the longitudinal plane.

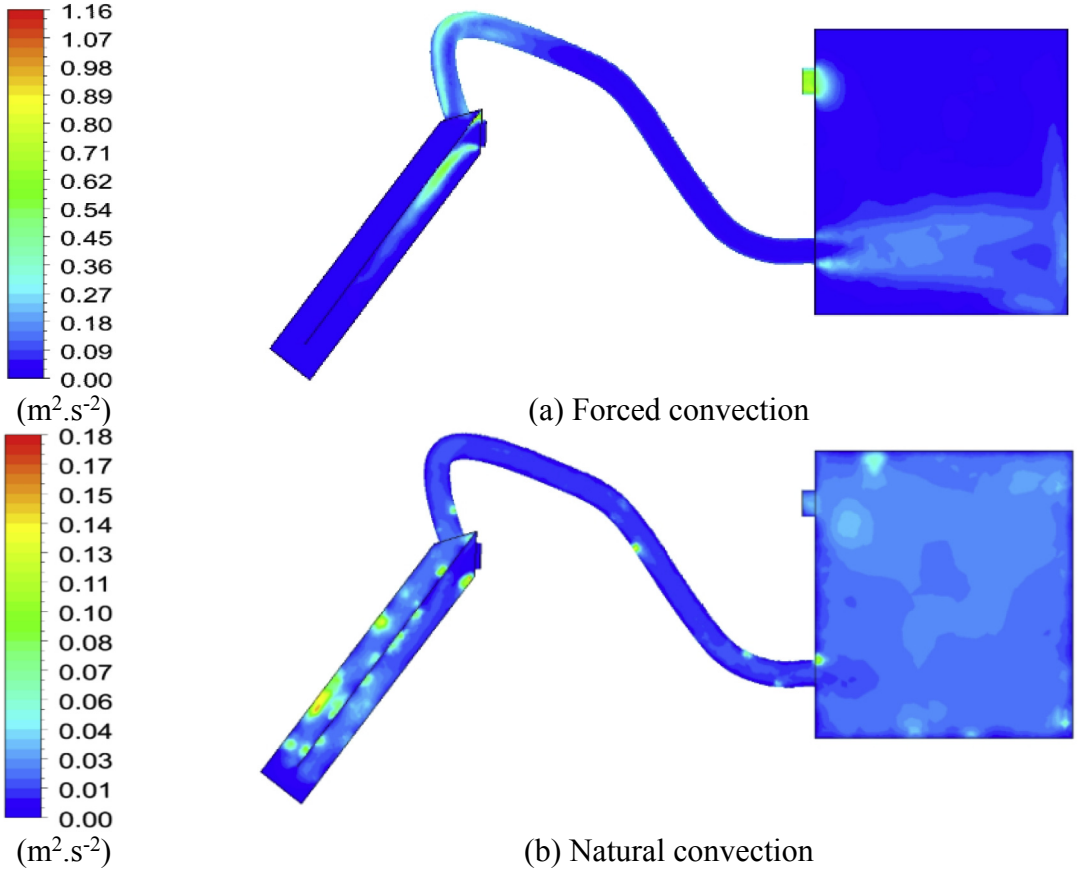

Fig. 10. Distribution of the turbulent kinetic energy in the longitudinal plane.

presents a weak value. With the flow progress inside the pipe, two small wake zones characteristic of the maximum values of the turbulent kinetic energy have been observed with two deviations. At the hole inlet of the box prototype, an expulsion area is invaded in the discharge area until the reverse wall. The wake zone characteristic of the maximum value of the turbulent kinetic energy has been observed below the box prototype and in the hole outlet with a value equal to $k = 0.04\ m^2\ s^{-2}$.

However, for the forced convection mode, a wake zone characteristic of the maximum value of the turbulent kinetic energy has been observed around the collector inlet of the SAH. This wake is expanded in the first passage near the absorber side and until the mid-plane. In these conditions, the maximum value of the turbulent kinetic energy is equal to $k = 0.96\ m^2\ s^{-2}$. Away from this area, the turbulent kinetic energy presents a very weak value excepting the lower leading edge of the absorber, where the turbulent kinetic energy is equal to $k = 0.09\ m^2\ s^{-2}$. At the exit of the second passage, a second wake zone characteristic of the maximum value of the turbulent kinetic energy appears and extends along the first part of the pipe connecting the SAH with the box prototype. After the decrease of the turbulent kinetic energy in the second part of the pipe, an expulsion area appears in the hole inlet of the box prototype and invaded in the discharge area until the reverse wall. This fact can be explained by the recirculation zone appeared in the whole area of the box prototype. Indeed, a slight decrease of the turbulent kinetic energy has been observed outside this area. However, in the outlet of the box prototype, a wake zone characteristic of the maximum value of the turbulent kinetic energy has been appeared.

4.7. Specific turbulent dissipation rate

Fig. 11 compares the specific turbulent dissipation rate distribution for the natural and the forced convection modes at $t = 14$ h in the longitudinal plane of the SAH supplying the box prototype. According to these results, it is clear that the choice of the convection mode presents a direct effect on the specific turbulent dissipation rate distribution. In fact, for the natural convection mode, a weak value of the specific turbulent dissipation rate has been observed in the hole inlet of the SAH. With the flow progress through the first and the second passages of the SAH, the specific turbulent dissipation rate keeps very low values with the exception of the walls of the insulation, the absorber, and the glass. In this side, the maximum value of the specific turbulent dissipation rate, appearing in the corner, is equal to $\omega = 460\ s^{-1}$. The same fact has been observed in the pipe connecting the SAH with the box prototype. The wake zone characteristic of the maximum value of the specific turbulent dissipation rate is located at the pipe walls on the concave side. In the hole inlet of the box prototype, a low expulsion area has been observed. However, in the whole area of the box prototype, the specific turbulent dissipation rate presents a low value. It is only at the level of the box prototype walls that the specific turbulent dissipation rate increases and reaches a moderate value equal to $\omega = 148\ s^{-1}$.

However, for the forced convection mode, a wake zone characteristic of the maximum value of the specific turbulent dissipation rate has been created from the collector inlet of the SAH, with a moderate value of the specific turbulent dissipation rate equal to $\omega = 308\ s^{-1}$. This wake is expanded in the first passage near the

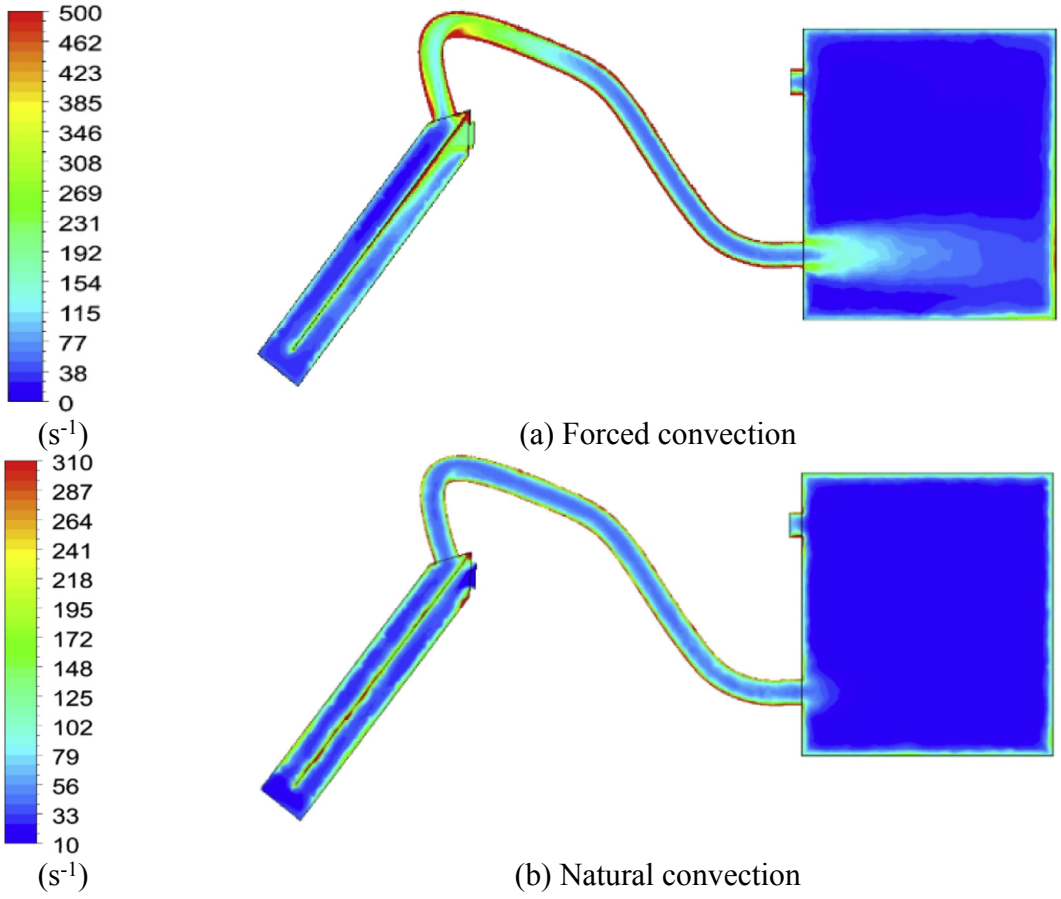

Fig. 11. Distribution of the specific turbulent dissipation rate in the longitudinal plane.

absorber side and until the mid-plane. In these conditions, the maximum value of the specific turbulent dissipation rate is equal to $\omega = 500\ s^{-1}$. Away from this area, the specific turbulent dissipation rate decreases and reaches a low value equal to $\omega = 38\ s^{-1}$ at the bottom of the collector where the insulator was localized. Through the second passage and away from the glass and the absorber, the specific turbulent dissipation rate continues the decrease even more and reaches a null value in the upper half plane. In the pipe connecting the SAH with the box prototype, the specific turbulent dissipation rate increases and reaches a maximum value equal to $\omega = 500\ s^{-1}$.

4.8. Turbulent viscosity

Fig. 12 compares the turbulent viscosity distribution for the natural and the forced convection modes at t = 14 h in the longitudinal plane of the SAH supplying the box prototype. According to these results, it is clear that the choice of the convection mode presents a direct effect on the turbulent viscosity distribution. In fact, for the natural convection mode, a weak value of the turbulent viscosity has been observed at the collector inlet of the SAH. Behind this area, a wake zone characteristic of the maximum value of the turbulent viscosity has been observed and expanded in the first passage near the absorber side. In these conditions, the maximum value of the turbulent viscosity is equal to $\mu_t = 0.002\ kg\ m^{-1}.s^{-1}$. Away from this area, the turbulent viscosity presents a very weak value. The same fact has been observed in the second passage, where the maximum value is equal to $\mu_t = 0.0009\ kg\ m^{-1}.s^{-1}$ in the first mid-plane. In the absorber, the turbulent viscosity reaches a weak value. At the exit of the second passage, a slight increase of the turbulent viscosity until $\mu_t = 0.003\ kg\ m^{-1}.s^{-1}$ has been observed in the first part of the pipe connecting the SAH with the box prototype. In the remainder of the pipe, the turbulent viscosity decreases and presents very low values. In the hole inlet of the box prototype, the low values of the turbulent viscosity continue to appear in the first part of the discharge area. In the second part, a slight increase of the turbulent viscosity has been noted on the side of the reverse wall. In the rest of the box prototype domain, a weak value of the turbulent viscosity has been observed. This fact can be explained by the recirculation zone appeared in the whole area of the box prototype. Indeed, a slight expansion of the turbulent viscosity until $\mu_t = 0.011\ kg\ m^{-1}.s^{-1}$ has been observed in the box prototype upper and the hole outlet.

However, for the forced convection mode, a wake zone characteristic of the maximum value of the turbulent viscosity has been observed around the collector inlet of the SAH. This wake is expanded in the first passage near the absorber side. In these conditions, the maximum value of the turbulent viscosity is equal to $\mu_t = 0.0023\ kg\ m^{-1}.s^{-1}$. Away from this area, the turbulent viscosity presents a very weak value. The same fact has been observed in the second passage, where the maximum value is equal to $\mu_t = 0.003\ kg\ m^{-1}.s^{-1}$ in the first mid-plane. In the absorber, the turbulent viscosity reaches a null value. At the exit of the second passage, a slight increase of the turbulent viscosity until $\mu_t = 0.0014\ kg\ m^{-1}.s^{-1}$ has been observed in the first part of the pipe connecting the SAH with the box prototype. In the remainder of the pipe, the turbulent viscosity decreases and presents very low values. In the holes inlet of the box prototype, the low values of the turbulent viscosity continue to appear in the first part of the discharge area. In the second part, a slight increase of the turbulent

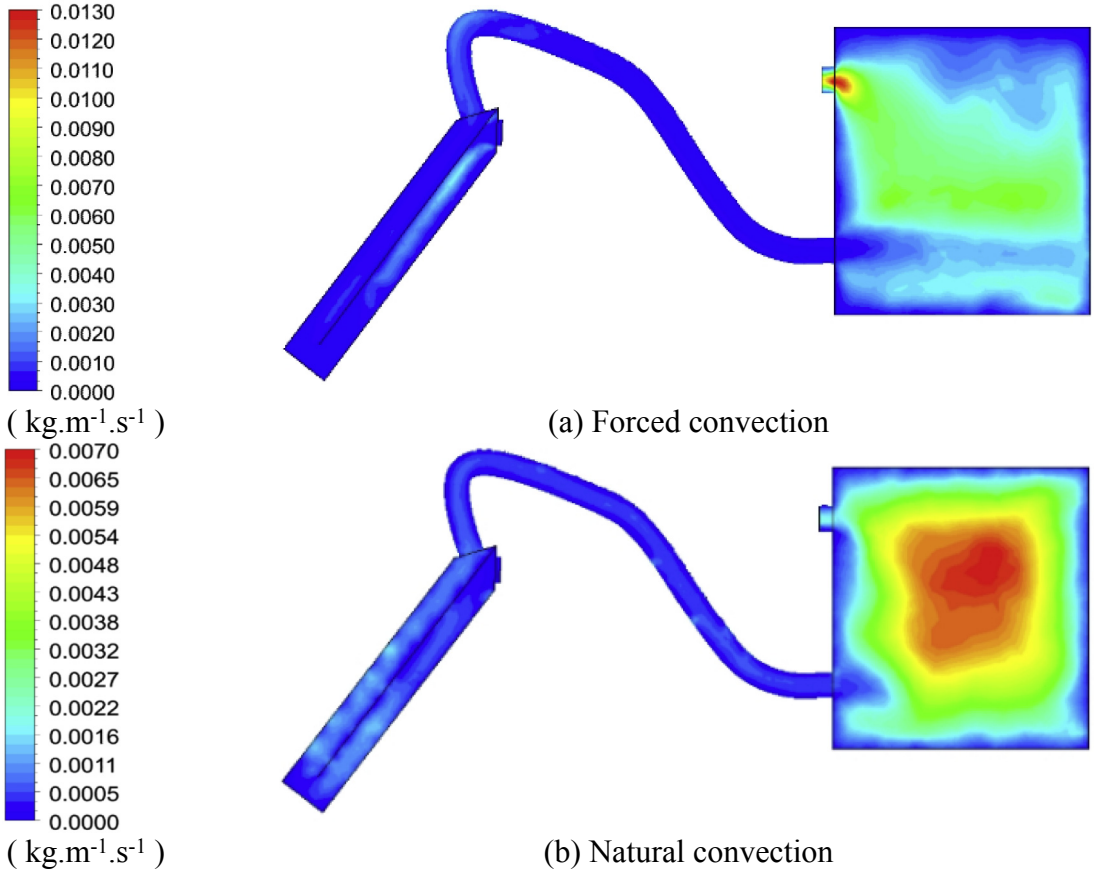

Fig. 12. Distribution of the turbulent viscosity in the longitudinal plane.

viscosity has been observed on the side of the reverse wall. In the rest of the box prototype domain, a wake zone characteristic of the maximum value of the turbulent viscosity, equal to $\mu_t = 0.007\ kg\ m^{-1}.s^{-1}$, has been created. This fact can be explained by the recirculation zone appeared in the whole area of the box prototype. Indeed, a rapid expansion of the turbulent viscosity until $\mu_t = 0.012\ kg\ m^{-1}.s^{-1}$ has been observed in the holes outlet of the box prototype.

4.9. Energy efficiency

Fig. 13 compares the profile of the energy efficiency over the time for the natural and the forced convection modes. According to these results, the energy efficiency presents very low values at the beginning of the day. With the increase of the temperature through the day, there is a gradual increase of the energy efficiency until $t = 12$ h, with a value equal to $\eta = 8.93\%$ for the natural convection mode and $\eta = 31.8\%$ for the forced convection mode. In the first half day, it has been noted that the increase of the energy efficiency is more important after $t = 10$ h. Afternoon, the energy efficiency starts to decrease with a constant slope.

5. Conclusion

Since the SAH is not very commonly used in the domestic and industrial applications, we are interested in the design and the realization of a new SAH test bench to investigate the efficiency of the solar system and the study of the turbulent flow with natural and forced convection. The considered test bench consists of two passages SAH separated by an absorber and powered by a fan working in a delivery mode and placed in the inlet, side the insulation. On the glass side, it is connected to the box prototype through a pipe. On this system, a glass is hanging on the front side and an absorber is inserted inside. The hot air flow is routed towards the box prototype. Two circular holes are located on the same face of the box prototype. The inlet hole allows the hot air supply. However, the outlet hole allows its escape into the ambient environment. The comparison between the natural and the forced convection modes confirms that the velocity and the turbulence characteristics are higher in the forced convection mode. However, the temperature is higher in the natural convection mode. For the energy efficiency, it presents very low values in the natural mode.

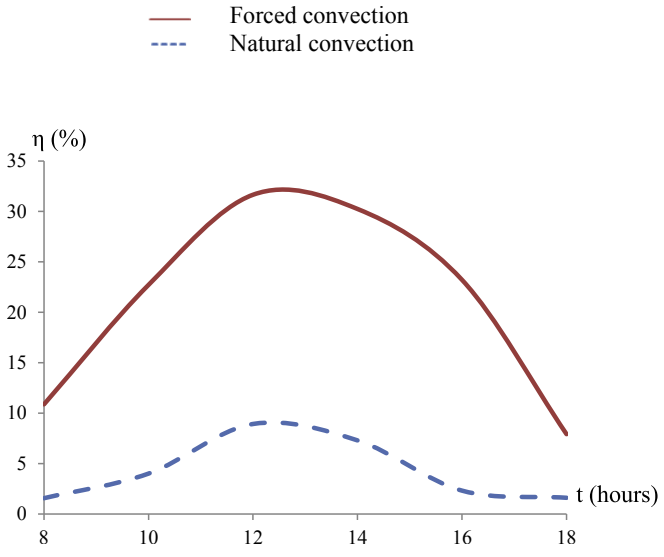

Fig. 13. Energy efficiency profile.

For this, we recommend the use of the forced convection mode since it can provide sustainable energy and substitute the expensive traditional technologies.

Nomenclature

A	Area of the SAH (m^2)
a	Absorption coefficient (dimensionless)
a_λ	Spectral absorption coefficient (dimensionless)
C_1	model constant (dimensionless)
C_p	Specific heat of the fluid ($J.kg^{-1}.K^{-1}$)
C_f	Specific heat of the fluid ($J.kg^{-1}.K^{-1}$)
E	Total energy (J)
F_i	Force component son the i direction (N)
G_k	Generation of the turbulent kinetic energy ($kg.m^{-1}.s^{-3}$)
G_ω	Generation of the dissipation rate of the turbulent kinetic energy ($kg.m^{-1}.s^{-3}$)
H	Height (m)
h	Thermal enthalpy ($J.kg^{-1}$)
I	Solar radiation ($W.m^{-2}$)
$I_{b\lambda}$	Black body intensity given by the Planck function ($W.m^{-2}$)
I_λ	Spectral intensity ($W.m^{-2}$)
$\vec{J}_j$	Diffusion flux of species j ($m^{-2}.s^{-1}$)
K_a	Absorption coefficient (m^{-1})
K_{eff}	Effective conductivity ($W.m^{-1}.K^{-1}$)
K	Turbulent kinetic energy ($m^2.s^{-2}$)
l	Length (m)
$\dot{m}$	Mass flow rate ($kg.s^{-1}$)
p	Pressure (Pa)
P_r	Prandtl number (dimensionless)
Q_H	Heat source or sink per unit volume ($kg.m^{-1}.s^{-3}$)
q_i	Diffusive heat flux (J)
Re	Reynolds number (dimensionless)
R_k	Constant of the k-ω turbulence model (dimensionless)
R_ω	Constant of the k-ω turbulence model (dimensionless)
$\vec{r}$	Position vector (m)
S_ω	Source terms of the specific turbulent dissipation rate ($kg.m^{-1}.s^{-3}$)
S_k	Source terms of the turbulent kinetic energy ($kg.m^{-1}.s^{-3}$)
s	Path length (m)
s_i^h	Source term (K)
s_i^T	Source term (K)
$\vec{s}$	Direction vector (dimensionless)
$\vec{s}'$	Scattering direction vector (dimensionless)
T_{out}	Outlet temperature (K)
T_{in}	Inlet temperature (K)
t	Time (s)
U	Free-stream velocity ($m.s^{-1}$)
u_i	Velocity components ($m.s^{-1}$)
u_i'	Fluctuating velocity components ($m.s^{-1}$)
V	Magnitude velocity ($m.s^{-1}$)
x_i	Cartesian coordinate (m)
x	Cartesian coordinate (m)
y	Cartesian coordinate (m)
Y_M	Fluctuating dilatation in compressible turbulence ($kg.m^{-1}.s^{-3}$)
Y_k	Turbulence dissipation of k ($kg.m^{-1}.s^{-3}$)
Y_ω	Turbulence dissipation of ω ($kg.m^{-1}.s^{-3}$)
z	Cartesian coordinate (m)
ΔV	Control volume (m^3)
η	Energy efficiency (%)

α_0	Constant of the k-ω turbulence model (dimensionless)
α_∞	Constant of the k-ω turbulence model (dimensionless)
$\alpha^*\infty$	Constant of the k-ω turbulence model (dimensionless)
δ_{ij}	Kronecker delta function (dimensionless)
μ	Dynamic viscosity (Pa.s)
μ_t	Turbulent viscosity (Pa.s)
μ_{eff}	Effective viscosity (Pa.s)
μ_{ij}^T	Coefficient term (dimensionless)
λ	Wave length (m)
ω	Specific dissipation rate (s^{-1})
ρ	Density ($kg.m^{-3}$)
β_I	Constant of the k-ω turbulence model (dimensionless)
σ	Stefan-Boltzmann constant ($W.m^{-2}.K^{-4}$)
σ_k	Turbulent Prandtl number for k (dimensionless)
σ_s	Scattering coefficient (dimensionless)
σ_ω	Turbulent Prandtl number for ω (dimensionless)
τ_{ij}	Viscous shear stress tensor (Pa)
$(\tau_{ij})_{eff}$	Deviatoric stress tensor (Pa)
Φ	Equivalence ratio (dimensionless)
φ	Phase function (°)
Γ_k	Effective diffusivity of k (Pa.s)
Γ_ω	Effective diffusivity of ω (Pa.s)
Ω	Swirl number (dimensionless)
Ω_{ij}	Rate of rotation tensor (s^{-1})
Ω'	Solid angle (°)

Abbreviations

SAH	Solar air heater
CFD	Computational fluid dynamic

References

[1] Yang M, Yang X, Li X, Wang Z, Wang P. Design and optimization of a SAH with offset strip fin absorber plate. Appl Energy 2014;113:1349–62.

[2] Altaa D, Bilgilib E, Ertekina C, Yaldiza O. Experimental investigation of three different SAHs: energy and exergy analyses, vol. 87; 2010. p. 2953–73.

[3] Zukowski M. Experimental investigations of thermal and flow characteristics of a novel microjet air solar heater. Appl Energy 2015;142:10–20.

[4] El-Sebaii AA, Aboul-Enein S, Ramadan MRI, Shalaby SM, Moharram BM. Thermal performance investigation of double pass-finned plate solar air-heater. Appl Energy 2011;88:1727–39.

[5] Wazed MA, Nukman Y, Islam MT. Design fabrication of a cost effectiveSAH for Bangladesh. Appl Energy 2010;87:3030–6.

[6] Sopian K, Alghoul MA, Ebrahim MA, Sulaiman MY, Musa EA. Evaluation of thermal efficiency of double-pass solar collector with porous- non-porousmedia. Renew Energy 2009;34:640–5.

[7] Esen H. Experimental energy and exergy analysis of a double-flow solar air-heater having different obstacles on absorber plates. Build Environ 2008;43:1046–54.

[8] Ozgen F, Esen M, Esen H. Experimental investigation of thermal perform-anceof a double-flow SAH having aluminum cans. Renew Energy 2009;34:2391–8.

[9] Chen L, Zhang XR. Experiments on natural convective solar thermal achieved by supercritical CO2/dimethyl ether mixture fluid. J Sol Energy Eng 2014;136:031011.

[10] Zhang XR, Zhang Y, Chen L. Experimental study on solar thermal conversion based on supercritical natural convection. Renew Energy 2014;62:610–8.

[11] Chen L, Zhang XR. Experimental analysis on a novel solar collector system achieved by supercritical CO2 natural convection. Energy Convers Manag 2014;77:173–82.

[12] Hassan H, Abo-Elfadl S. Experimental study on the performance of double pass and two inlet ports SAH (SAH) at different configurations of the absorber plate. Renew Energy 2018;116:728–40.

[13] Alam MR, Zain MFM, Kaish ABMA, Jamil M. Underground soil and thermal conductivity materials based heat reduction for energy-efficient building in tropical environment. Indoor Built Environ 2015;24:185–200.

[14] Goodarzi M, Nouri E. A new double-pass parallel-plate heat exchanger with better wall temperature uniformity under uniform heat flux. Int J Therm Sci 2016;102:137–44.

[15] Singh S, Dhiman P. Thermal performance of double pass packed bed SAHs–A comprehensive review. Renew Sustain Energy Rev 2016;53:1010–31.

[16] Driss Z, Mlayeh O, Driss D, Maaloul M, Abid MS. Numerical simulation and experimental validation of the turbulent flow around a small incurved Savonius wind rotor. Energy 2014;74:506–17.

[17] Driss Z, Mlayah O, Driss S, Driss D, Maaloul M, Abid MS. Study of the bucket design effect on the turbulent flow around unconventional Savonius wind rotors. Energy 2015;89:708–29.

[18] Driss Z, Mlayah O, Driss S, Maaloul M, Abid MS. Study of the incidence angle effect on the aerodynamic structure characteristics of an incurved Savonius wind rotor placed in a wind tunnel. Energy 2016;113:894–908.

[19] ANSYS. Fluent theory guide. Southpointe 2600, ANSYS Drive Canonsburg, PA: ANSYS, Inc.; 2016. 15317.

[20] Tiwari GN, Sahota L. Advanced solar-distillation systems: basic principles, thermal modeling, and its application. Springer; 2017.

[21] Prałat K. Research on thermal conductivity of the wood and analysis of results obtained by the hot wire method. Exp Tech 2015.